



Contents lists available at ScienceDirect

# Engineering Science and Technology, an International Journal

journal homepage: [www.elsevier.com/locate/jestch](http://www.elsevier.com/locate/jestch)



## Trajectory planning of deep-cutting laser profiling of superabrasive profile grinding wheels

Hui Deng <sup>a,\*</sup>, Chuan He <sup>a</sup>, Weiqi Liu <sup>b</sup>, Wei Xiong <sup>c</sup>

<sup>a</sup> Hunan Provincial Key Laboratory of High Efficiency and Precision Machining of Difficult-to-Cut Material, School of Mechanical Engineering, Hunan University of Science and Technology, Xiangtan 411201, China

<sup>b</sup> Hunan Yintao Precision Manufacturing Co., Ltd., Hengyang 421007, China

<sup>c</sup> Hunan Traditional Chinese Medical College, Zhuzhou 412012, China

### ARTICLE INFO

#### Keywords:

Superabrasive  
Profile grinding wheels  
Laser dressing  
Profiling efficiency  
Deep-cutting dressing  
Trajectory planning

### ABSTRACT

The low profiling efficiency is the key barrier to the industrial application of laser dressing technology for profile grinding wheels. In this paper, the trajectory planning method of deep-cutting laser profiling was proposed for the first time, the theoretical model of the energy distribution of the Gaussian laser beam on the surface of the profile grinding wheel was established, and the effect of this method on improving the profiling efficiency of superabrasive profile grinding wheel was systematically studied. Through comparative experiments, it was confirmed that the trajectory planning method could effectively improve the profiling efficiency of the V-shaped grinding wheel, and it was found that the smaller the tip angle, the greater the efficiency improvement. The change of grain size will lead to the change of grain removal method, which will affect the profiling efficiency of V-shaped grinding wheel, but it has little influence on the profiling accuracy. The V-tip arc radius of the diamond grinding wheel with a particle size of 20–180 μm after laser profiling could be controlled between 10 and 20 μm, which was difficult to achieve by mechanical or electrical dressing method. The trajectory planning method could also significantly improve the profiling efficiency of convex/concave arc-shaped grinding wheels, and the greater the arc radius or chord-to-diameter ratio of the grinding wheel, the greater the efficiency improvement. Even though convex/concave arc-shaped grinding wheels were the same size, their profiling efficiency and material removal efficiency were quite different. For grinding wheels with different arc radii or chord-to-diameter ratios, different process strategies should be selected during laser profiling to ensure a comprehensive balance between efficiency, accuracy and quality.

### 1. Introduction

Grinding process based on superabrasive profile grinding wheel is the preferred means to achieve high-efficiency and high-performance machining of complex curved surface parts [1,2]. During grinding, there is a certain mapping relationship between the surface contour accuracy of the grinding wheel and the surface accuracy of the processed workpiece, and the surface micro-topography of the grinding wheel will also affect the surface and sub-surface quality of the processed workpiece [3,4]. Dressing is a key link to improve the surface contour accuracy and micro-topography of the grinding wheel, thereby improving the grinding accuracy and quality [5,6]. However, due to the complex axial sectional contour, extremely high hardness of the grain, and high strength of the bond, it is very difficult to precisely dress superabrasive

profile grinding wheels, especially coarse-grained profile grinding wheels [7,8].

In order to solve this problem, many scholars have developed multiple methods that can be used to dress superabrasive profile grinding wheels. Among them, the most widely used methods are mechanical method and electrical dressing methods (including electrical discharge dressing and electrolytic in-process dressing), but they still have many disadvantages and limitations. For example, the traditional mechanical method has defects such as fast tool wear and difficult compensation, high dust concentration, and great harm. Even more tricky, the mechanical method is difficult to dress the concave surface grinding wheels because the dressing tools tend to interfere with the surface of the profile grinding wheel [9]. Non-metallic bond and all kinds of grains are non-conductive, which prevents in the top of the excessively protruding

\* Corresponding author.

E-mail address: [denghnu@163.com](mailto:denghnu@163.com) (H. Deng).

grains being cut off during the dressing process. Therefore, the electrical dressing methods cannot precisely dress the coarse-grained superabrasive profile grinding wheels and face problems such as difficult waste liquid treatment and heavy pollution [10,11].

Laser dressing is considered to be the most applicable and most environment-friendly technology [12–14]. Zhou et al. [15–17] pointed out that it has the advantages of non-contact and high controllability, and is especially suitable for dressing superabrasive profile grinding wheels with complex axial sectional contours. Laser dressing is usually divided into two processes: profiling and sharpening. The laser beam usually has three incident modes: quasi-tangential, radial, or deep-cutting, as shown in Fig. 1(a). The laser dressing technology was proposed by Ramesh Babu et al. [18,19] in the late 1980s, and many scholars have extensively explored the laser sharpening of parallel grinding wheels. However, there are few reports on the research related to laser profiling, especially the profiling of profile grinding wheels. The research group of Professor Konrad Wegener, former chairman of the Scientific Technical Committee STC-G of the International Academy for Production Engineering (CIRP), has been engaged in research of laser dressing technology for a long time. The research group [20] took the metal-vitrified CBN profile grinding wheel (the axial sectional contour line was composed of arc-shaped lines, V-shaped lines, rectangular lines, and other curves) as the object to confirm the feasibility of the quasi-tangential laser profiling method based on multiple layering and layer-by-layer cutting. Although the surface contour accuracy of the grinding wheel after profiling using this method was high, this method had the disadvantage of low profiling efficiency. This was because as the surface material of the grinding wheel was continuously removed, more and more laser energy would directly pass through the surface of the grinding wheel and cause losses, resulting in a sharp reduction in the laser power density value irradiated on the surface of the grinding wheel during profiling, and the profiling efficiency was greatly reduced. In order to improve the profiling efficiency, the research group [21] also proposed a composite process of radial rough profiling and quasi-tangential fine profiling. After about 5 h, a parallel diamond grinding wheel was profiled into a trapezoidal grinding wheel, and it was found that the surface shape accuracy of the grinding wheel could reach  $\pm 3 \mu\text{m}$  after profiling. In order to overcome the disadvantages of low efficiency of the quasi-tangential profiling method, our research group [22,23] explored the evolution law of laser incident angle, irradiated spot area, and irradiated power density with laser cutting depth in the early stage, and thus proposed the deep-cutting laser profiling method. Using this method, it took about 4.5 h to profile a diamond parallel grinding wheel with a grain size of about  $180 \mu\text{m}$  into an arc-shaped grinding wheel. To sum up, the laser method can be used to dress all kinds of superabrasive

profile grinding wheels, but it currently has the bottleneck of low profiling efficiency, which has become a key barrier hindering the industrial application of laser dressing technology of profile grinding wheels.

As shown in Fig. 1(b), taking the deep-cutting laser method to profile a parallel grinding wheel into a V-shaped grinding wheel as an example, when the Gaussian laser beam scans from point A to point C along the trajectory line, the defocus amount  $\Delta$  gradually increases due to the existence of the focus characteristic, and the laser incident angle  $\alpha$  gradually increases due to the decreasing of the cutting depth  $c_p$ , so that the laser spot area  $S_p$  irradiated on the surface of the grinding wheel increases continuously, and the laser power density deposited in the irradiated area continues to decrease, which eventually leads to a gradual decrease in material removal efficiency and laser profiling efficiency. When the laser power density is lower than the material removal threshold (let  $B$  be the intersection point between the center line of the laser beam and the trajectory line at this time), the laser beam will not be able to remove the material and lose the profiling ability, that is, the laser beam will be in the idling state when scanning from point B to point C. Therefore, planning the scanning trajectory scientifically is essential to improve the efficiency of deep-cutting laser profiling of superabrasive profile grinding wheels.

In this paper, we will explore the precise planning method of the profiling trajectory of the profile grinding wheel, establish a theoretical model of the energy distribution of the Gaussian laser beam on the surface of the profile grinding wheel, and systematically study the effect of this method on improving the profiling efficiency of the superabrasive profile grinding wheel and the influence of grinding wheel geometry and grain size on efficiency improvement.

## 2. Experimental conditions

Fig. 2 is a schematic of the laser profiling experimental setup. When conducting the plasma spectrum collection experiment in Section 3.1, the resin-bonded diamond grinding wheel was selected as the experimental material. The grain size  $d$  of the grinding wheel was about  $100 \mu\text{m}$  ( $150^{\#}$ ), the outer diameter  $R$  was about 75 mm, and the width  $W$  was about 8.3 mm. In order to facilitate the observation of the microtopography, ring-shaped resin-bonded diamond grinding wheel blocks were selected as the experimental material in all profiling experiments. In the profiling experiment of the V-shaped grinding wheel in Section 3.2.1, grinding wheel blocks with an outer diameter  $R$  of about 85 mm, a width  $W$  of about 9.0 mm, and a grain size  $d$  of about  $120 \mu\text{m}$  were selected. In the profiling experiment of the V-shaped grinding wheel in Section 3.2.2, grinding wheel blocks with outer diameter  $R$  of about 88

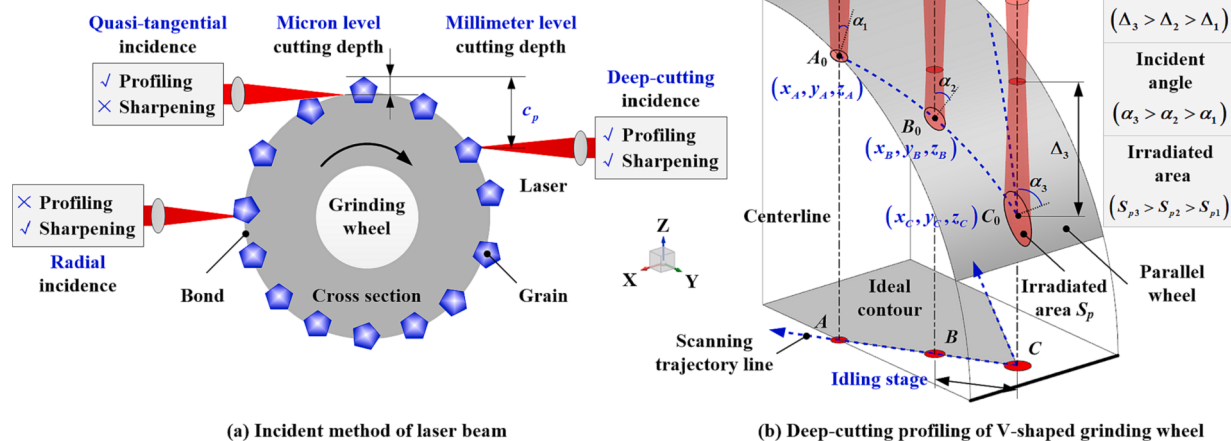


Fig. 1. Schematic of laser beam incident and scanning method.

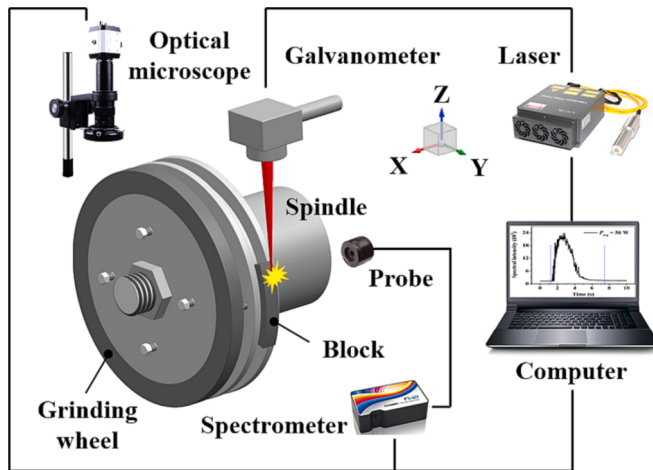


Fig. 2. Schematic of the laser profiling experimental setup.

mm, width  $W$  of about 8.46 mm, and grain sizes  $d$  of about 180  $\mu\text{m}$  (80 $^{\#}$ ), 125  $\mu\text{m}$  (120 $^{\#}$ ), 38  $\mu\text{m}$  (400 $^{\#}$ ), and 23  $\mu\text{m}$  (600 $^{\#}$ ) were selected. The grain size  $d$  of grinding wheel blocks selected in the profiling experiment of the arc-shaped grinding wheel in Section 3.3 was about 125  $\mu\text{m}$  (120 $^{\#}$ ), the outer diameter  $R$  was about 85 mm, and the width  $W$  was about 9.0 mm.

The grinding wheel and grinding wheel block were fixed on the mechanical spindle which can realize the linear movement of the X-Y axis through the flange. The power of the laser (model YLPN-1-20x120-100) used in the experiment was  $P_{avg} = 20\text{-}70 \text{ W}$ , the repetition frequency  $f = 50 \text{ kHz}$ , the pulse width  $\tau = 20 \text{ ns}$ , the focal spot radius  $r_0 = 14 \mu\text{m}$ , and the wavelength  $\lambda = 1064 \text{ nm}$ . The laser beam was transmitted by the optical fiber to the inside of the galvanometer (model SCANCUBE III-10) fixed on the Z-axis electric displacement platform, and it could scan the surface of the grinding wheel or grinding wheel block with a rotational speed  $n$  of 420 r/min according to the set trajectory and speed under the control of the galvanometer. A fiber optic spectrometer (model FLA4000) was used to collect the plasma spectral signals during the ablation process, and an optical microscope (model AM4515T), scanning electron microscope (model JSM-IT100), and other instruments were used to observe the axial sectional contour and surface topography of the grinding wheel and the grinding wheel block after profiling.

### 3. Results and discussions

#### 3.1. Profiling trajectory planning

##### 3.1.1. Trajectory planning method

Fig. 3 is a schematic diagram of deep-cutting laser profiling of V-shaped grinding wheel. Before profiling, the galvanometer is adjusted along the Z-axis so that the focal plane of the laser beam just passes through the point with the maximum Z coordinate value on the intersection line of the grinding wheel surface (the target position in Fig. 3). The intersection line refers to the connecting line of each intersection point of the centerline of the laser beam and the surface of the grinding wheel when the laser beam scans along the V-shaped trajectory. During profiling, the grinding wheel rotates at a constant speed, and the laser beam scans back and forth along the trajectory at a constant speed. With the progress of the profiling process, the Z coordinate value of each point on the intersection line and the target position are constantly changing. Therefore, during the profiling process, it is also necessary to control the galvanometer to feed intermittently along the negative direction of the Z-axis, so that the focal plane of the laser beam is relocated to the target position periodically, and finally, the parallel grinding wheel can be profiled into a V-shaped grinding wheel.

The V-shaped grinding wheel is symmetrical along the axis, and one side was selected for analysis. According to Fig. 1(b), it can be seen that when the laser beam scans along the trajectory line AC and crosses the critical point B, the laser beam will enter the idling stage and cannot remove the material. Therefore, in theory, if the line segment  $l_i$  between the starting point A and the critical point B is used as the scanning trajectory line, the idle stroke can be eliminated and the profiling efficiency can be improved. However, during the profiling process, the starting point A remains unchanged, but the critical point B gradually approaches point C with the movement of the focal plane of the laser beam. Therefore, every time the focal plane is fed along the negative direction along the Z-axis once, the scanning trajectory needs to be re-planned, which will lead to cumbersome planning steps and increase the difficulty of operation. In order to simplify the technological process and take into account the profiling efficiency, a trajectory line  $\Delta l_i$  is appropriately added to the theoretical trajectory line  $l_i$ , so that the scanning trajectory needs to be re-planned after the feeding distance of the focal plane reaches  $\Delta d$ . According to the pre-experimental exploration, it is more reasonable to take  $\Delta d$  as 2.9 mm (about 5 times the Rayleigh length of the laser beam). When the sizes of the parallel grinding wheel before profiling and the V-shaped grinding wheel after profiling are determined, the focal plane is located in the plane with the Z coordinate values  $\Delta z\text{-}\Delta d$ ,  $\Delta z\text{-}2\Delta d$ , ...,  $\Delta z\text{-}N\Delta d$  in turn, and the lengths of each profiling trajectory obtained by planning are  $l_1 + \Delta l_1$ ,  $l_2 + \Delta l_2$ , ...,

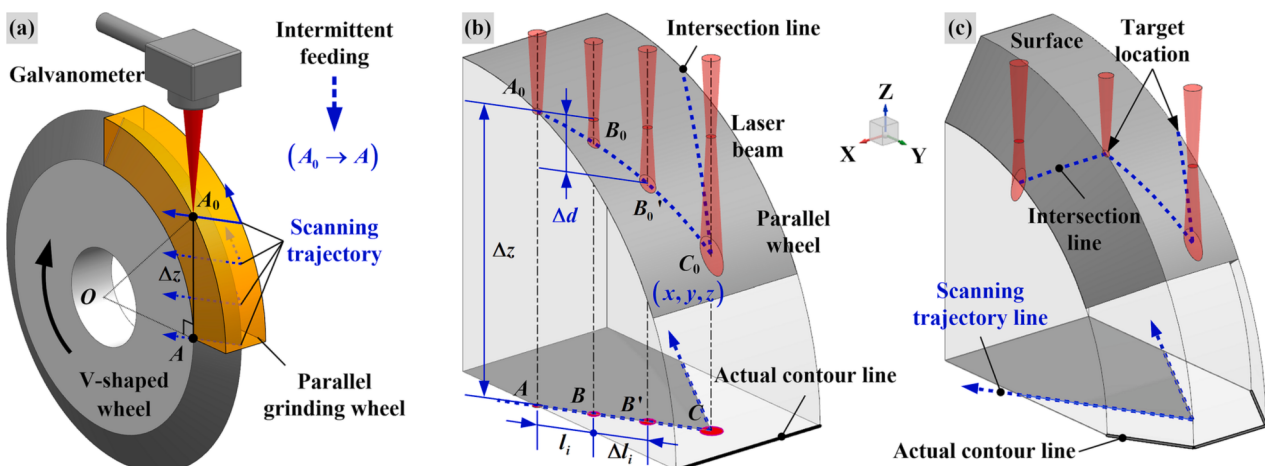


Fig. 3. Deep-cutting laser profiling of V-shaped grinding wheel. (a) Laser beam intermittent feeding, (b) Laser profiling stage 1, (c) Laser profiling stage 2.

$l_N + \dots + \Delta l_N$  respectively. When point  $B'$  reaches point  $C$ , the profiling trajectory planning is completed, as shown in Fig. 3(b)–(c).

### 3.1.2. Laser power density

When the focal plane of the laser beam is at different positions, the laser power density at each point on the intersection line of the grinding wheel surface is calculated and compared with the material removal threshold of the grinding wheel to find the critical point  $B$  on the scanning trajectory line, which is the essence of profiling trajectory planning. Therefore, how to calculate the laser power density is one of the key points in trajectory planning.

Before profiling, the equation of the parallel grinding wheel surface can be expressed as:

$$z^2 = R^2 - y^2 \quad (1)$$

In the formula,  $R$  is the radius of the parallel grinding wheel. Let:

$$f(x, y, z) = -R^2 + y^2 + z^2 \quad (2)$$

The normal vector at any point on the grinding wheel surface is:

$$\vec{n} = \left\{ \frac{\partial f}{\partial x}, \frac{\partial f}{\partial y}, \frac{\partial f}{\partial z} \right\} = \{0, 2y, 2z\} \quad (3)$$

The laser incident angle  $\alpha$  refers to the angle between the centerline of the laser beam and the outer normal of the grinding wheel surface at the laser incident point. The upper surface of the parallel grinding wheel (that is, the surface of the grinding wheel above the XOY plane in Fig. 3(a)) was selected for analysis, the centerline of the laser beam is parallel to the Z-axis, and its unit vector is  $\vec{m} = \{0, 0, 1\}$ . According to the formula for calculating the angle between vectors  $\vec{m} = \{m_x, m_y, m_z\}$  and  $\vec{n} = \{n_x, n_y, n_z\}$  shown in Eq. (4), the incident angle of the laser beam can be obtained by combining with Eq. (3). According to the literature [24], the absorptivity  $A_c$  of the grinding wheel material to the laser beam can be calculated according to Eq. (5), where  $i$  is the refractive index, and  $k$  is the extinction coefficient.

$$\cos\alpha = \cos(\widehat{\vec{m}, \vec{n}}) = \frac{m_x n_x + m_y n_y + m_z n_z}{\sqrt{m_x^2 + m_y^2 + m_z^2} \times \sqrt{n_x^2 + n_y^2 + n_z^2}} \quad (4)$$

$$A_c = 1 - \frac{(icos\alpha - 1)^2 + (kcos\alpha)^2}{2(icos\alpha + 1)^2 + 2(kcos\alpha)^2} - \frac{(i - \cos\alpha)^2 + k^2}{2(i + \cos\alpha)^2 + 2k^2} \quad (5)$$

When profiling the V-shaped grinding wheel, the equation of the scanning trajectory of the laser beam in the XOY plane can be expressed by Eq. (6), where  $\theta$  is the tip angle of the V-shaped grinding wheel,  $W$  is the width of the grinding wheel, and  $R_0$  is the radius at the end face of the V-shaped grinding wheel.

$$\begin{cases} y = -k\left(x + \frac{W}{2}\right) + R_0, -\frac{W}{2} \leq x < 0 \\ y = k\left(x - \frac{W}{2}\right) + R_0, 0 \leq x \leq \frac{W}{2} \\ k = \tan\left(\frac{180^\circ + \theta}{2}\right) \end{cases} \quad (6)$$

According to literature [25], in the cross-section where the Z coordinate is  $z$ , the spot equation of the fundamental-mode Gaussian laser beam is:

$$\begin{cases} (x - x_0)^2 + (y - y_0)^2 = r^2 \\ r = r_0 \sqrt{1 + \left(\frac{\lambda(z - z_0)}{\pi r_0^2}\right)^2} \end{cases} \quad (7)$$

In the formula,  $r_0$  is the spot radius of the laser beam at the focal plane (that is, the focal spot radius of the laser beam),  $z_0$  is the Z coordinate

value at the focal plane (the focal plane needs to be fed intermittently along the negative direction of the Z-axis during the profiling process, and the value should be set according to the position of the focal plane), and  $r$  is the spot radius of the laser beam at the Z coordinate of  $z$ .  $(x_0, y_0)$  is the coordinate of the intersection point between the centerline of the laser beam and the XOY plane, and the intersection point is located on the laser scanning trajectory line described by Eq. (6).

The equation for the upper surface of the parallel grinding wheel (above the XOY plane) can be expressed as:

$$z = \sqrt{R^2 - y^2} \quad (8)$$

The laser-irradiated area  $S_p$  refers to the area of the laser beam irradiated on the upper surface of the grinding wheel, and its calculation formula is:

$$\begin{cases} S_p = \iint_{D_{xy}} \sqrt{1 + \left(\frac{\partial z}{\partial x}\right)^2 + \left(\frac{\partial z}{\partial y}\right)^2} dx dy \\ \frac{\partial z}{\partial x} = 0 \\ \frac{\partial z}{\partial y} = -\frac{y}{\sqrt{R^2 - y^2}} \end{cases} \quad (9)$$

In the formula, the integration area  $D_{xy}$  is the projection area of the laser-irradiated spot in the XOY plane, which needs to be discussed and determined according to the position relationship between the projection of the laser beam spot and the parallel grinding wheel. When the projection of the spot falls completely inside the grinding wheel,  $D_{xy}$  can be expressed as:

$$D_{xy} : \begin{cases} x_0 - r \leq x \leq x_0 + r \\ -\sqrt{r^2 - (x - x_0)^2} + y_0 \leq y \leq \sqrt{r^2 - (x - x_0)^2} + y \end{cases} \quad (10)$$

When the projection of the spot exceeds the left boundary of the grinding wheel,  $D_{xy}$  can be expressed as:

$$D_{xy} : \begin{cases} -0.5W \leq x \leq x_0 + r \\ -\sqrt{r^2 - (x - x_0)^2} + y_0 \leq y \leq \sqrt{r^2 - (x - x_0)^2} + y \end{cases} \quad (11)$$

When the projection of the spot exceeds the right boundary of the grinding wheel,  $D_{xy}$  can be expressed as:

$$D_{xy} : \begin{cases} x_0 - r \leq x \leq 0.5W \\ -\sqrt{r^2 - (x - x_0)^2} + y_0 \leq y \leq \sqrt{r^2 - (x - x_0)^2} + y \end{cases} \quad (12)$$

When the projection of the spot exceeds the upper boundary of the grinding wheel,  $D_{xy}$  can be expressed as:

$$D_{xy} : \begin{cases} x_0 - r \leq x \leq x_0 + r \\ -\sqrt{r^2 - (x - x_0)^2} + y_0 \leq y \leq R \end{cases} \quad (13)$$

Considering the above four situations comprehensively, the integration area  $D_{xy}$  can finally be expressed as:

$$D_{xy} : \begin{cases} \max(-0.5W, x_0 - r) \leq x \leq \min(0.5W, x_0 + r) \\ -\sqrt{r^2 - (x - x_0)^2} + y_0 \leq y \leq \min(\sqrt{r^2 - (x - x_0)^2} + y_0, R) \end{cases} \quad (14)$$

According to the literature [26], the ratio  $\eta$  of the laser power incident on the surface of the grinding wheel to the laser output power can be expressed as:

$$\eta = \iint_{D_{xy}} \frac{3}{\pi r^2} \exp\left(\frac{-3((x - x_0)^2 + (y - y_0)^2)}{r^2}\right) dx dy \quad (15)$$

The laser power density  $I_p$  irradiated on the surface of the grinding wheel can be expressed by Eq. (16). The laser power density  $I_A$  is the product of

the irradiated power density  $I_p$  and the laser absorptivity  $A_c$ , which can be represented by Eq. (17). Substituting Eqs. (5) and (16) into Eq. (17), the laser power density  $I_A$  at each point on the intersection line of the grinding wheel surface can be calculated.

$$I_p = \frac{\eta P_{avg}}{S_p f \tau} \quad (16)$$

$$I_A = A_c \times I_p \quad (17)$$

### 3.1.3. Material removal threshold

How to determine the grinding wheel material removal threshold is another key point in trajectory planning. It is a common method to determine the removal threshold of grain or bond by carrying out laser ablation experiments of grinding wheel material, but this method is time-consuming and material-consuming, and its accuracy is not high [27]. During the laser dressing process, the plasma emission spectrum consisting of the weaker continuous background spectrum and the line spectrum superimposed on the background spectrum will be produced on the processing area of the grinding wheel surface. The line spectrum is emitted by the stimulated radiation produced by neutral atoms or ions in the plasma when they transition from a high-energy excited state to a lower energy level, that is, each line spectrum corresponds to a specific element in grinding wheel material. The intensity of the line spectrum is positively correlated with the corresponding element content, laser power density, and material removal rate. Therefore, the removal threshold of grain or bond can be determined by observing the characteristic spectral line and its intensity of the plasma during the dressing process with a spectrometer.

Under the condition of laser power of 40 W, the plasma emission spectrum signal with a wavelength in the range of 200–600 nm generated during laser ablation of diamond grain and resin bond were measured respectively, and the results are shown in Fig. 4. The diamond grain used in this experiment also included Fe, Ni, Mg, and other additive elements in addition to C element, and the phenolic resin bond also included Cu, Si, Mg and other filler elements in addition to C, H, and O elements. During the laser profiling process, the gasification removal temperature of the diamond grain is much higher than that of the resin bond, so the characteristic spectral line of the grain was selected to determine the removal threshold of the grinding wheel material. The line spectrum in Fig. 4 was calibrated by querying the atomic spectrum

database of the National Institute of Standards and Technology (NIST). It can be found that the wavelength of the spectral line of the grain was mainly concentrated between 350 and 600 nm, while the wavelength of the spectral line of the bond was concentrated between 200 and 450 nm. In order to avoid the interference of the bond spectral line, Ni I 515.576 with the wavelength between 450 and 600 nm and the highest peak spectral line intensity was selected as the characteristic spectral line in the grain spectral lines.

By adjusting the galvanometer, the focal plane of the laser beam just passed through point  $A_0$  on the surface of the parallel grinding wheel, as shown in Fig. 3(a). Under the conditions of 20 W, 50 W, and 70 W, respectively, the laser beam scanned the parallel grinding wheel at a speed of  $v_0 = 0.319$  mm/s along the trajectory line, and the characteristic spectral line Ni I 515.576 was collected continuously by a spectrometer, and the results are shown in Fig. 5. At time  $t_1$ , the laser beam contacted the surface of the grinding wheel and excited the characteristic spectral line; subsequently, the intensity of the characteristic spectral line first increased sharply and then gradually decreased, and both the width and peak intensity of the spectral line increased with the increase of power. From time  $t_2$ , the spectrometer could barely detect the characteristic spectral line, indicating that there was no material removal phenomenon. That was, a critical point (corresponding to point B in Fig. 1) appeared at time  $t_2$ , when the power density of the laser beam was just equal to the removal threshold of the diamond grain.

According to Eq. (17), the laser power density  $I_A$  at each point on the intersection line of the grinding wheel surface was calculated, and the results are shown in Fig. 6. From  $t_1$  to  $t_2$ , the scanning trajectory length  $L_t$  of the laser beam was  $v_0 (t_2 - t_1)$ , and according to Fig. 5,  $L_t$  was calculated to be 1.324 mm, 1.994 mm, and 2.345 mm, respectively. When the power was 20 W, 50 W, and 70 W, according to Fig. 6, it could be seen that  $I_A$  gradually decreased from  $6.52 \times 10^8$  W/cm<sup>2</sup>,  $16.31 \times 10^8$  W/cm<sup>2</sup>, and  $22.83 \times 10^8$  W/cm<sup>2</sup>, respectively, and when it reached the critical point B, its values were  $2.98 \times 10^7$  W/cm<sup>2</sup>,  $3.07 \times 10^7$  W/cm<sup>2</sup>, and  $2.97 \times 10^7$  W/cm<sup>2</sup>, respectively. After that, the laser beam could not remove material and was in the idling stage, and its power density continued to decrease and finally approached zero. It could be found that the grain removal thresholds determined under different power conditions by the spectral monitoring method were basically close, indicating that the method had good reliability. The  $I_A$  at the critical point B was averaged, and finally the removal threshold of the diamond grain was determined to be  $3.0 \times 10^7$  W/cm<sup>2</sup>.

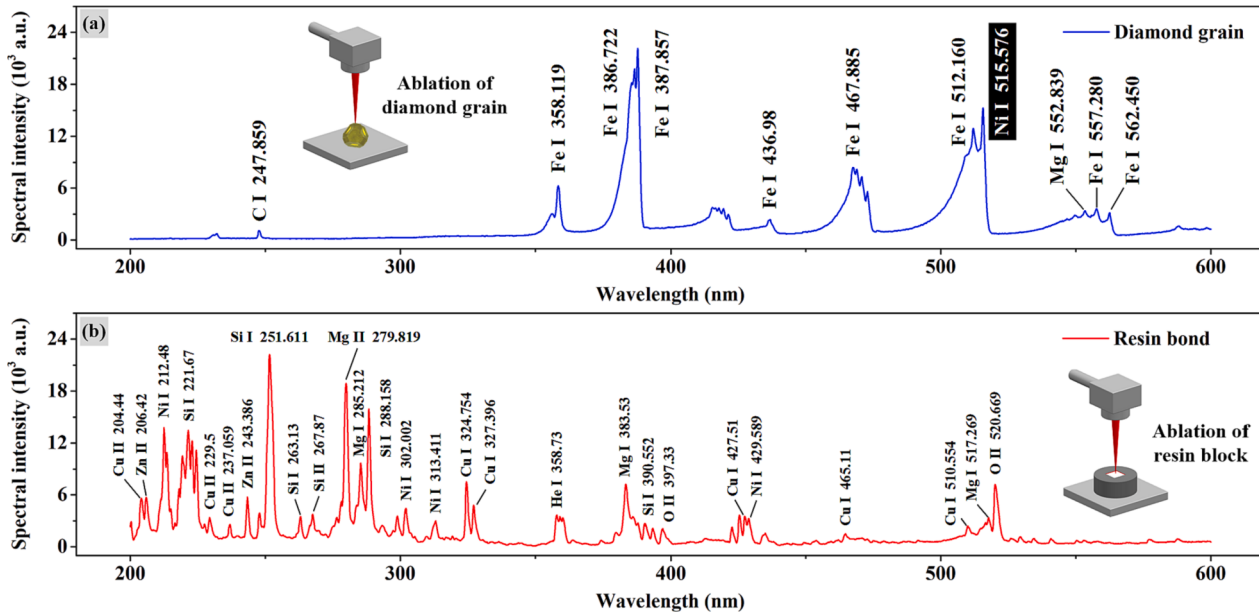


Fig. 4. Plasma spectroscopy during laser ablation of diamond and resin. (a) Diamond grain, (b) Resin bond.

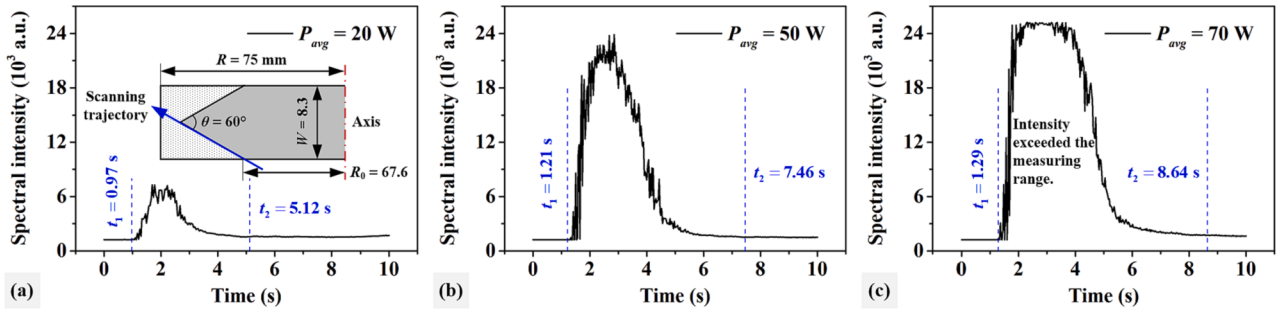


Fig. 5. Characteristic spectral line intensity during resin-bonded diamond grinding wheel profiling. (a)  $P_{avg} = 20\text{ W}$ , (b)  $P_{avg} = 50\text{ W}$ , (c)  $P_{avg} = 70\text{ W}$ .

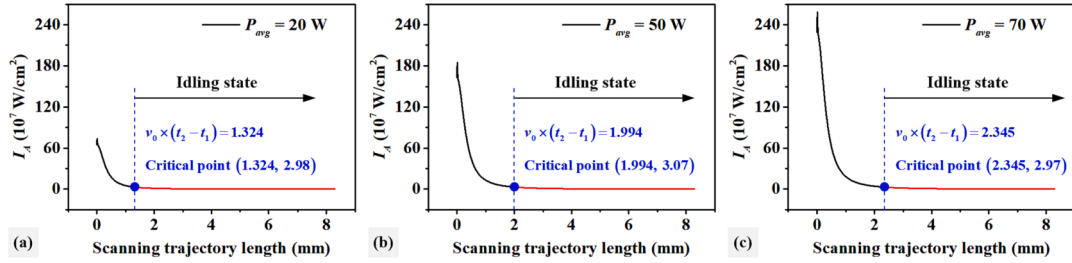


Fig. 6. Laser power density at each point on the intersection line. (a)  $P_{avg} = 20\text{ W}$ , (b)  $P_{avg} = 50\text{ W}$ , (c)  $P_{avg} = 70\text{ W}$ .

### 3.1.4. Trajectory planning verification

In this section, taking the profiling of a parallel grinding wheel into a V-shaped grinding wheel as shown in Fig. 7(a) as an example, the reliability of the above profiling trajectory planning method was verified by means of spectral measurement. The verification process was performed in two steps. In the first step, according to the method described in Section 3.1.1, the Z coordinate values of the focal plane of the laser beam were set to  $\Delta z$ ,  $\Delta z-\Delta d$ ,  $\Delta z-2\Delta d$ , ...,  $\Delta z-N\Delta d$  ( $\Delta z = 24.73\text{ mm}$ ,  $\Delta d = 2.9\text{ mm}$ ) in sequence. The laser power density  $I_A$  (laser power  $P_{avg} = 70\text{ W}$ ) at each point on the intersection line of parallel grinding wheel surfaces was calculated using the method described in Section 3.1.2. The  $I_A$  at each point on the intersection line was compared with the grain removal threshold determined in Section 3.1.3, so that the critical points  $B$  and  $B'$  (Fig. 3(b)) were found on the scanning trajectory line  $AC$ , and finally the theoretical length  $L_i$  of each profiling trajectory and the total number  $N$  of trajectory planning were determined. The results are shown in Fig. 7 and Table 1.

In the second step, the measurement experiment of the characteristic spectral lines in the laser profiling process of the V-shaped grinding wheel was carried out. The focal plane of the laser beam was placed in the plane with the Z coordinate values  $\Delta z$ ,  $\Delta z-\Delta d$ ,  $\Delta z-2\Delta d$ , ...,  $\Delta z-6\Delta d$  ( $\Delta z = 24.73\text{ mm}$ ,  $\Delta d = 2.9\text{ mm}$ ) in turn, and the laser beam with a power of 70 W was controlled by the galvanometer to scan the surface of the parallel grinding wheel once at a speed of  $v_1 = 0.325\text{ mm/s}$  along the trajectory shown in Fig. 7(a). The intensity of the characteristic

spectral line Ni I 515.576 was collected synchronously by using a spectrometer, and the results are shown in Fig. 8. When the laser beam started to contact the surface of the grinding wheel and excited the characteristic spectral line, this time was recorded as the starting time  $t_0$  of the profiling trajectory. When the intensity of the characteristic spectral line first increased and then decreased to the critical intensity value (about 1600), there was basically no material removal in the laser-irradiated area, and this time was recorded as the termination time  $t_f$  of the profiling trajectory. Based on this, the measured length  $L_j$  of each profiling trajectory was determined, and the results are shown in Table 1.

It could be seen from Table 1 that the degree of agreement between the theoretical value  $L_i$  and the measured value  $L_j$  of each profiling trajectory was relatively high, and the maximum deviation between the two was less than 15%. The main reasons for the deviation are: (1) During multiple measurements, as the focal plane of the laser beam moves intermittently along the negative direction of the Z-axis, the peak power density on the intersection line of the grinding wheel surface gradually decreases (Fig. 7), resulting in a gradual decrease in the peak intensity of the characteristic spectral line collected each time (Fig. 8); (2) The fall time of the spectrometer will affect the measurement of the trajectory length. The peak intensity of the characteristic spectral line of the first few trajectories is relatively large, the fall time of the spectrometer is longer, and the measured termination time  $t_f$  is delayed compared with the termination time of laser ablation, resulting in a

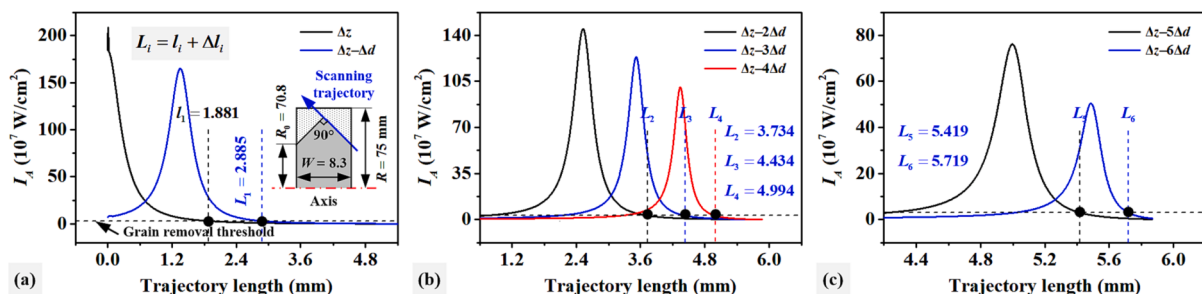
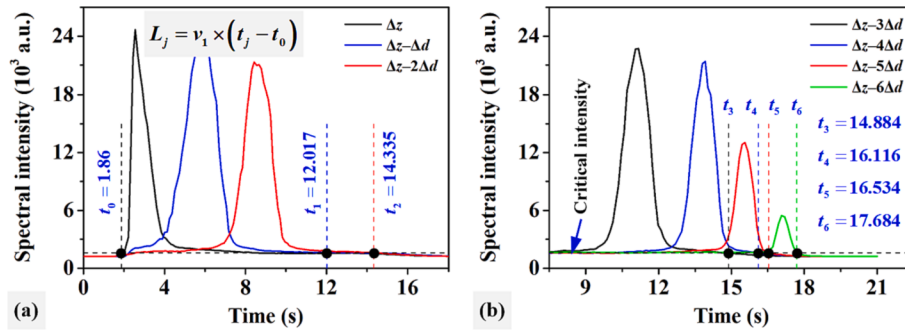


Fig. 7. Laser power density at each point on the intersection line at different focal plane positions.

**Table 1**

Theoretical and measured trajectory length.

| No. | Theoretical length (mm) |              |       | Measured length<br>$L_j$ (mm) | Deviation (%) |
|-----|-------------------------|--------------|-------|-------------------------------|---------------|
|     | $l_i$                   | $\Delta l_i$ | $L_i$ |                               |               |
| 1   | 1.881                   | 1.004        | 2.885 | 3.301                         | 14.4          |
| 2   | 2.885                   | 0.849        | 3.734 | 4.054                         | 8.57          |
| 3   | 3.734                   | 0.700        | 4.434 | 4.233                         | 4.53          |
| 4   | 4.434                   | 0.560        | 4.994 | 4.633                         | 7.23          |
| 5   | 4.994                   | 0.425        | 5.419 | 4.769                         | 12.0          |
| 6   | 5.419                   | 0.300        | 5.719 | 5.143                         | 10.1          |

**Fig. 8.** Characteristic spectral line intensity of laser ablation at different focal plane positions.

slight increase in the measured value of the trajectory compared with its actual value. The peak intensities of the characteristic spectral lines of the last few trajectories are smaller, the fall time of the spectrometer is shortened, and the measured termination time  $t_j$  is advanced, resulting in a slight decrease in the measured value of the trajectories.

### 3.2. V-shaped grinding wheel profiling

#### 3.2.1. Profiling efficiency comparison

In order to verify the effectiveness and superiority of the trajectory planning method in improving the profiling efficiency, a comparative experiment of deep-cutting laser profiling of V-shaped grinding wheel was carried out in this section. The laser power used in the experiment was  $P_{avg} = 70$  W, and the laser scanning speed  $v_2 = 0.322$  mm/s. In order to ensure that the initial conditions were as consistent as possible, two sets of experiments were carried out on the surface of the same parallel grinding wheel block. The surface of the grinding wheel block was equally divided into two areas along its axial direction, and laser profiling was carried out in the left area by adopting the segmented trajectory scanning method. According to the size of the parallel grinding wheel and the V-shaped grinding wheel, the profiling trajectory in the left area was planned into 7 segments by using the method described in Section 3.1, and the length of each profiling trajectory is shown in Table 2. In the area on the right side of the grinding wheel block surface, laser profiling was performed by adopting the entire

trajectory scanning method, and the length of the scanning trajectory was the same as that of the seventh trajectory in Table 2, which was 6.24 mm. It can be found that when profiling the right area, it takes about 19.4 s for the laser beam to scan along the entire trajectory each time. However, at the initial stage of profiling, the laser beam is in a state of idling for about 10.5 s each time, and the material cannot be removed. As the profiling process progresses, the idle time is gradually shortened, the profiling efficiency of the right area is gradually improved, and finally the profiling efficiency of the left and right areas will tend to be consistent.

The grinding wheel block was fixed on the flange shown in Fig. 2, and the focal plane of the laser beam was moved to point  $A_0$  (Fig. 3(a)) on the surface of the grinding wheel block, and then the laser profiling experiments were carried out in the above two ways. When profiling the left area, the laser beam was first cyclically scanned along the first trajectory in Table 2, and the focal plane of the laser beam was periodically adjusted to feed intermittently along the negative direction of the Z-axis. When the cumulative feed distance reached  $\Delta d$ , the laser scanning trajectory was switched to the second one. Switched periodically in this way until the seventh profiling trajectory in Table 2 was completed. Whenever a trajectory was completed, the profiling time and the axial sectional contour of the grinding wheel block were recorded, and the results are shown in Fig. 9. It can be found that when profiling the left area, the volume of material to be removed was about 2824 mm<sup>3</sup>, which took 3.28 h, and the material removal efficiency was 14.34 mm<sup>3</sup>/min.

**Table 2**

Length of each profiling trajectory.

| Segmented trajectory | Number | $l_i$ | $\Delta l_i$ | $L_i$ | Number | $l_i$ | $\Delta l_i$ | $L_i$ |
|----------------------|--------|-------|--------------|-------|--------|-------|--------------|-------|
| Entire trajectory    | 1      | 1.837 | 1.015        | 2.852 | 5      | 5.095 | 0.495        | 5.590 |
|                      | 2      | 2.852 | 0.879        | 3.731 | 6      | 5.590 | 0.381        | 5.971 |
|                      | 3      | 3.731 | 0.745        | 4.476 | 7      | 5.971 | 0.269        | 6.240 |
|                      | 4      | 4.476 | 0.619        | 5.095 |        |       |              |       |

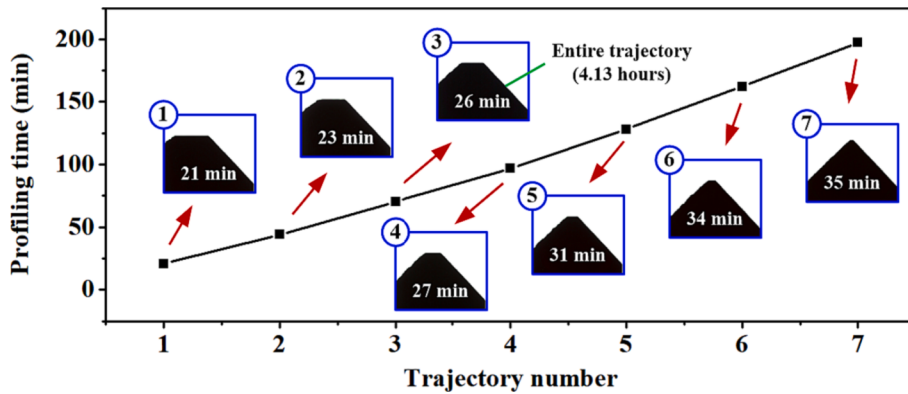


Fig. 9. Time consumption and axial sectional contour of each profiling stage.

While when the entire trajectory scanning method was used to complete the profiling of the right area, the volume of material to be removed was about  $2824 \text{ mm}^3$ , which took 4.13 h, and the material removal efficiency was  $11.39 \text{ mm}^3/\text{min}$ . This showed that the trajectory planning method can shorten the profiling time by 0.85 h and improve the profiling efficiency by more than 20%. It should be noted that under the premise that the size of the parallel grinding wheel remains unchanged, the increase in efficiency will also be affected by the geometric size and grain size of the V-shaped grinding wheel. See Section 3.2.2 for details.

### 3.2.2. Influence of tip angle and grain size on profiling efficiency

In this section, the influence of the tip angle  $\theta$  and the grain size  $d$  of the V-shaped grinding wheel on trajectory planning, profiling efficiency, and precision was explored. When the laser beam with a power of 50 W scanned along the trajectory line  $AC$  at a speed of  $v_2 = 0.322 \text{ mm/s}$ , under the condition of different tip angles  $\theta$ , the incident angle  $\alpha$  and laser power density  $I_A$  at each point on the intersection line of the grinding wheel surface were calculated, and the results are shown in Fig. 10. It can be seen that under different  $\theta$  conditions,  $\alpha$  and  $I_A$  showed the same variation trend, the former gradually increased to  $86.1^\circ$ , while the latter gradually decreased and finally stabilized, but the variation ranges of  $\alpha$  and  $I_A$  were different. For example, when  $\theta = 15^\circ$ ,  $AC = 3.24 \text{ mm}$  (each scan took 100.6 s),  $\alpha$  gradually increased from  $39.2^\circ$ ,  $I_A$  gradually decreased from  $2.7 \times 10^9 \text{ W/cm}^2$ , dropped to the grain removal threshold after about 18.6 s, and finally stabilized at  $2.6 \times 10^8 \text{ W/cm}^2$ ; When  $\theta = 150^\circ$ ,  $AC = 4.4 \text{ mm}$  (each scan took 13.7 s),  $\alpha$  gradually increased from  $80.0^\circ$ ,  $I_A$  gradually decreased from  $7.0 \times 10^8 \text{ W/cm}^2$ , dropped to the grain removal threshold after about 4.8 s, and

finally stabilized at  $6.4 \times 10^5 \text{ W/cm}^2$ . It can be seen that the smaller the tip angle of the V-shaped grinding wheel, the larger the peak value, the smaller the valley value, and the larger the variation of the laser power density on the intersection line. It can be inferred that the smaller the tip angle, the more the number of profiling trajectories, and the greater the improvement of the profiling efficiency by the trajectory planning method. In addition, in order to achieve close material removal efficiency and profiling accuracy, a grinding wheel with a large tip angle requires higher laser power than a grinding wheel with a small tip angle in the initial stage of profiling. While in the later stage of profiling, it is just the opposite, that is, a grinding wheel with a small tip angle requires higher laser power than a grinding wheel with a large tip angle.

Eight parallel grinding wheel blocks (two blocks for each grain size) with grain sizes of about  $180 \mu\text{m}$ ,  $125 \mu\text{m}$ ,  $38 \mu\text{m}$ , and  $23 \mu\text{m}$  were clamped on the flange shown in Fig. 2, and the profiling trajectory was planned into 10 segments by using the method described in Section 3.1, and then the deep-cutting laser profiling experiment of V-shaped grinding wheel ( $\theta = 60^\circ$ ) was carried out simultaneously under the same conditions. After the third profiling trajectory was completed, one grinding wheel block of each grain size was removed, and the surface topography was observed with a scanning electron microscope. The results are shown in Fig. 11(a)–(d). In Fig. 11(a) and (b), the grain size ( $d = 180 \mu\text{m}$ ,  $125 \mu\text{m}$ ) was relatively large, and most of the grains were removed by the laser beam through graphitization, gasification, or cracking. In Fig. 11(c) and (d), the grain size ( $d = 38 \mu\text{m}$ ,  $23 \mu\text{m}$ ) was relatively small, and the laser beam loosened the grains by removing the bond around the grains, and some grains fell off as a whole under the action of centrifugal force (without directly consuming laser energy).

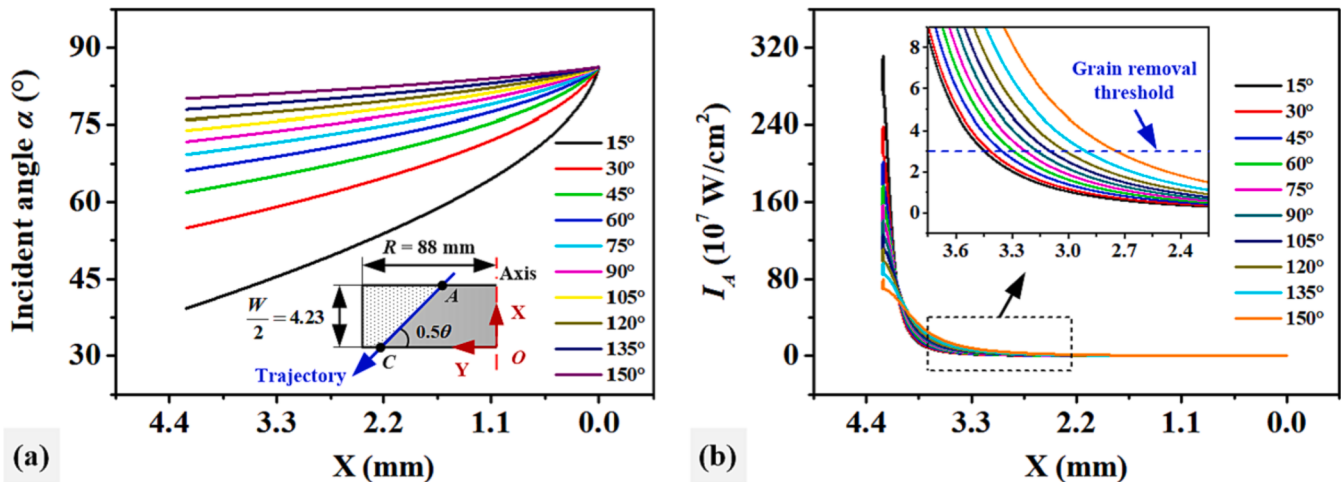


Fig. 10. Influence of tip angle on (a) the incident angle and (b) power density of laser beam.

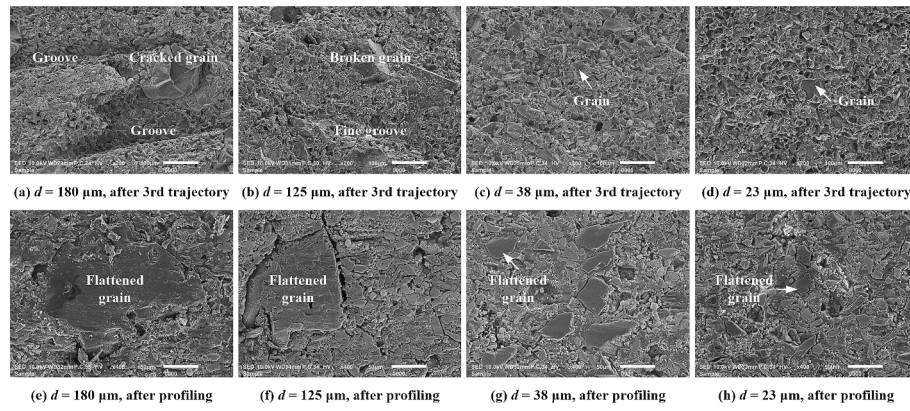


Fig. 11. Surface micro-topography of V-shaped grinding wheel at different profiling stages.

Therefore, as the grain size decreases, the removal method of grains will gradually change from crushing removal to falling-off removal, the material removal efficiency and laser profiling efficiency will gradually increase, and the grinding wheel surface can obtain higher contour accuracy faster.

After the experiment, the observation results of the surface topography of the remaining four grinding wheel blocks are shown in Fig. 11 (e)–(h). It can be seen that the top of the excessively protruding grains (including small-sized grains) was flattened by the laser beam, and the cracking or falling off of the grains rarely occurred. The surface of the grains and the bond was very smooth, and the surface flatness of each grinding wheel block was significantly improved compared with the completion of the third trajectory. It can be seen from the theoretical calculation and spectral monitoring results in Figs. 7–8 that in the initial stage of profiling, the peak power density on the intersection line of the grinding wheel surface is higher, and a higher material removal efficiency can be achieved at this time, but the profiled surface roughness is higher (Fig. 11(a)–(d)). As the profiling process progresses, the laser power density at each point on the intersection line of the grinding wheel surface will gradually decrease, resulting in a gradual decline in profiling efficiency; however, due to the gradual increase of the incident angle (close to 90° in the later stage of profiling), the incident mode of the laser beam gradually changes from a deep-cutting to a quasi-tangential direction, so the profiling accuracy is gradually improved

(Fig. 11(e)–(h)). This shows that deep-cutting laser profiling is a processing process of “fast first, then slow, rough first, then fine” [22], which can achieve an adaptive balance between efficiency and precision.

The tip angle  $\theta$  and the arc radius  $r_t$  of the tip are the core indicators for evaluating the contour accuracy of the V-shaped grinding wheel [28]. The axial sectional contour of the profiled grinding wheel block was observed by an optical microscope, and the results are shown in Fig. 12. The images were further preprocessed, segmented, edge extracted and data fitted, and the tip angles of the four V-shaped grinding wheel blocks were about 59.83°, 60.07°, 60.15°, and 60.01°, respectively, and the arc radii of the tips were about 18.4 μm, 15.5 μm, 12.6 μm, and 13.9 μm, respectively. It can be found that since the laser beam can directly cut the top of the excessively protruding grains (Fig. 11), the grain size has little effect on the laser profiling accuracy. Mechanical method or electrical dressing methods (including electrical discharge dressing and electrolytic in-process dressing) usually achieve the purpose of profiling by removing the bond and making the loose grains fall off directly. Therefore, the limit value of the arc radius of the tip of the V-shaped grinding wheel after profiling by these two methods is equivalent to the grain size (the larger the grain size, the larger the arc radius of the tip, and the lower the profiling accuracy). The laser method can break through the limitation of the grain size on the profiling accuracy. After the diamond grinding wheel with a grain size of 180 μm

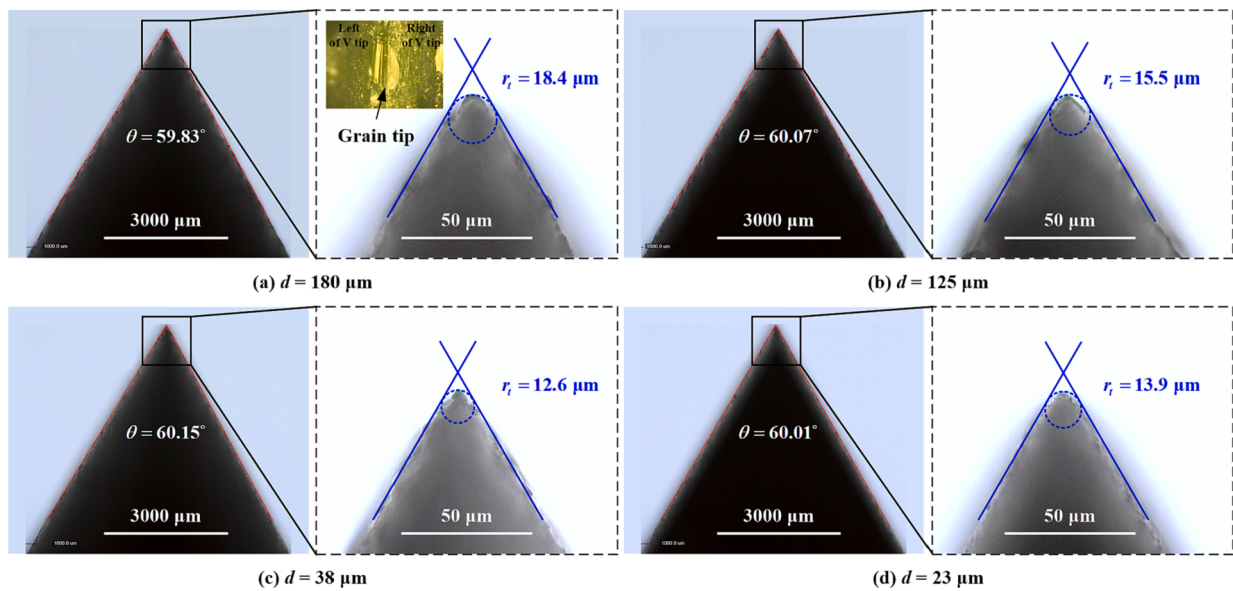


Fig. 12. Axial sectional contour accuracy of grinding wheel after profiling.

was profiled by the laser method, the arc radius of the V-shaped tip was only about 1/10 of the grain size. It can be seen that compared with the mechanical method or the electric dressing method, the laser method has a significant advantage in the dressing accuracy of the coarse-grained grinding wheel.

### 3.3. Arc-shaped grinding wheel profiling

#### 3.3.1. Profiling trajectory planning

Arc-shaped grinding wheels and V-shaped grinding wheels are the two most commonly used types of profile grinding wheels. In Sections 3.1 and 3.2, we studied the profiling trajectory planning method by taking the V-shaped grinding wheel as an example. In this section, the feasibility of applying this method to arc-shaped grinding wheel profiling will be explored. Fig. 13 is a schematic diagram of deep-cutting laser profiling of a convex/concave arc-shaped grinding wheel. Before profiling, the focal plane of the laser beam passed through point  $A_0$  by adjusting the galvanometer along the Z-axis direction. During profiling, the laser beam scanned the surface of the grinding wheel reciprocally at a constant speed  $v_2 = 0.322 \text{ mm/s}$  along the arc-shaped trajectory, and was periodically controlled by the galvanometer to feed intermittently along the negative direction of the Z-axis, and finally the parallel grinding wheel could be profiled into a convex/concave arc-shaped grinding wheel.

The profiling trajectory planning method of the arc-shaped grinding wheel is basically the same as that of the V-shaped grinding wheel in Section 3.1. It is only necessary to replace the equation of the laser scanning trajectory line shown in Eq. (6). As shown in Fig. 14, in the XOY plane, the equation of the scanning trajectory can be expressed by Eq. (18) when profiling a convex arc-shaped grinding wheel, and the equation of scanning trajectory when profiling a concave arc-shaped grinding wheel can be expressed by Eq. (19).

$$\begin{cases} y = a + \sqrt{r_c^2 - x^2}, -\frac{W}{2} \leq x \leq \frac{W}{2} \\ a = R_0 - \sqrt{r_c^2 - \left(\frac{W}{2}\right)^2} \end{cases} \quad (18)$$

In the formula,  $r_c$  is the radius of the convex arc,  $a$  is the distance from the center of the convex arc to the coordinate origin  $O$ ,  $W$  is the width of the grinding wheel, and  $R_0$  is the radius at the end face of the grinding wheel.

$$\begin{cases} y = a - \sqrt{r_c^2 - x^2}, -\frac{W}{2} \leq x \leq \frac{W}{2} \\ a = R_0 + \sqrt{r_c^2 - \left(\frac{W}{2}\right)^2} \end{cases} \quad (19)$$

In the formula,  $r_c$  is the radius of the concave arc,  $a$  is the distance from the center of the concave arc to the coordinate origin  $O$ ,  $W$  is the width of the grinding wheel, and  $R_0$  is the radius at the end face of the grinding wheel.

The arc-shaped grinding wheel has symmetry along the axis direction, and the surface on the right side of the Y-axis in Fig. 14 was taken for analysis. When the focal plane passed through point  $A_0$  (Fig. 13) and the laser beam with a power of 70 W scanned along the trajectory line  $AC$ , the laser-irradiated area  $S_p$ , laser incident angle  $\alpha$ , and laser power density  $I_A$  at each point on the intersection line of the grinding wheel surface were calculated, and the results are as shown in Fig. 15. For the convex arc-shaped grinding wheel, when the laser beam scan from point  $A$  to point  $C$ ,  $S_p$  showed an upward trend in the range of  $1184.7 \mu\text{m}^2$ – $7.4 \text{ mm}^2$  (the focal spot area of the laser beam was about  $615.8 \mu\text{m}^2$ ),  $\alpha$  gradually increased from  $74.9^\circ$  to  $87.2^\circ$ , and  $I_A$  decreased rapidly from  $1.66 \times 10^9 \text{ W/cm}^2$  and finally tended to be stable. As for the concave arc-shaped grinding wheel, the three just showed the opposite trend of change,  $S_p$  showed a downward trend in the range of  $4.1 \text{ mm}^2$ – $2369.4 \mu\text{m}^2$ ,  $\alpha$  gradually decreased from  $87.2^\circ$  to  $74.9^\circ$ , and  $I_A$  gradually increased to  $1.47 \times 10^9 \text{ W/cm}^2$  and then tended to be stable. It can be found that for convex/concave arc-shaped grinding wheels of the same size, although the variation range of the laser power density is basically the same, the variation rate is quite different (the time from the peak value to the critical value was 3.3 s and 9.5 s, respectively), which will result in a different number of planned profiling trajectories (the number of concave arc-shaped grinding wheels is less than that of convex arc grinding wheels).

The profiling trajectory was planned using the method described in Section 3.1, and deep-cutting laser profiling experiments of convex/concave arc-shaped grinding wheels were carried out on the device shown in Fig. 2. The time consumption and the axial sectional contour of the grinding wheel after the completion of each profiling trajectory were recorded, and the results are shown in Table 3. It can be found that when profiling the convex arc-shaped grinding wheel, the volume of material removed was about  $3745 \text{ mm}^3$ , which took 3.55 h, and the material removal rate was  $17.58 \text{ mm}^3/\text{min}$ , which was a significant improvement compared with the material removal rate when we used the entire trajectory scanning method to profile the convex arc-shaped grinding wheel in the literature [23]. When profiling the concave arc-shaped grinding wheel, the volume of material removed was about  $10194 \text{ mm}^3$ , which took 5.05 h, and the material removal rate was  $33.64 \text{ mm}^3/\text{min}$ , which was nearly twice that of processing convex arc-shaped grinding wheels. The reason for this difference is that, as can be seen from Fig. 15(c), when profiling a concave arc-shaped grinding wheel, the laser power density is the highest at point  $C$  on the trajectory line (about  $1.47 \times 10^9 \text{ W/cm}^2$ ), and it changes gently near point  $C$ , which can be maintained for a long time in high position; while profiling a convex arc-shaped grinding wheel, although the peak power density is

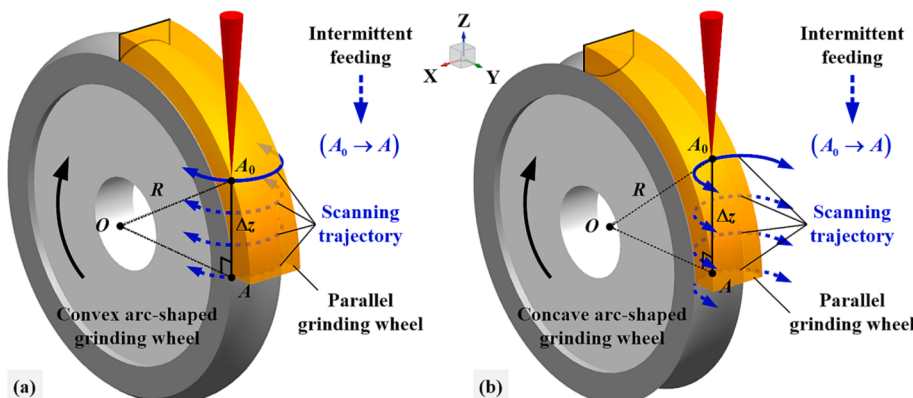


Fig. 13. Schematic of deep-cutting laser profiling of convex/concave arc-shaped grinding wheel.

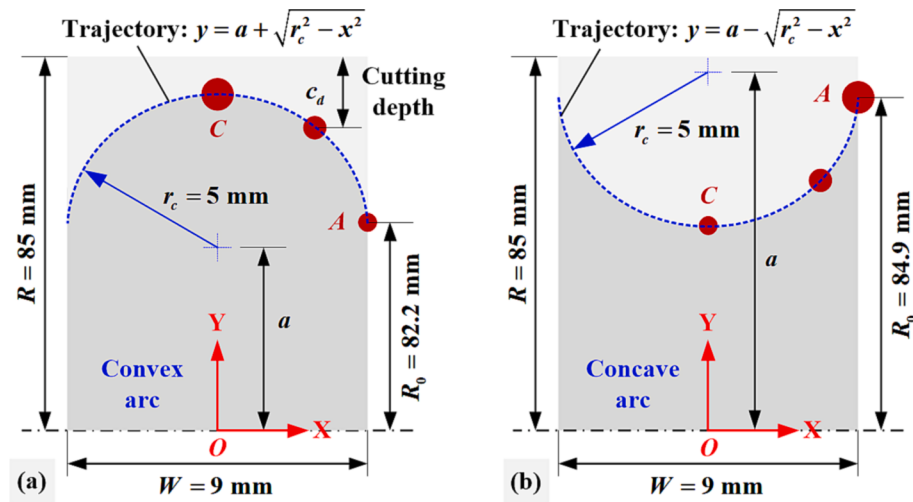


Fig. 14. Scanning trajectory of the laser beam. (a) Convex arc-shaped grinding wheel, (b) Concave arc-shaped grinding wheel.

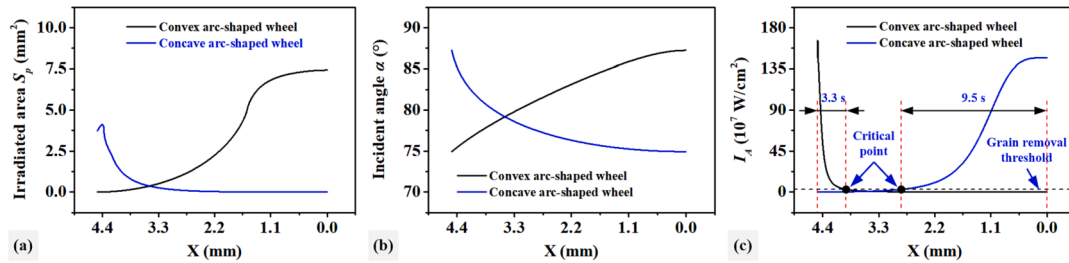


Fig. 15. Variation law of (a) irradiated area, (b) incident angle, and (c) laser power density.

Table 3

Trajectory length, time consumption and sectional contour of each profiling stage.

| Convex arc-shaped grinding wheel |                   |            |         | Concave arc-shaped grinding wheel |                   |            |         |
|----------------------------------|-------------------|------------|---------|-----------------------------------|-------------------|------------|---------|
| Number                           | $L_i (\text{mm})$ | Time (min) | Contour | Number                            | $L_i (\text{mm})$ | Time (min) | Contour |
| 1                                | 1.787             | 28         |         | 1                                 | 3.887             | 49         |         |
| 2                                | 2.487             | 32         |         | 2                                 | 4.488             | 57         |         |
| 3                                | 3.170             | 35         |         | 3                                 | 4.933             | 63         |         |
| 4                                | 3.853             | 37         |         | 4                                 | 5.258             | 65         |         |
| 5                                | 4.580             | 40         |         | 5                                 | 5.599             | 69         |         |
| 6                                | 5.599             | 41         |         |                                   |                   |            |         |

as high as  $1.66 \times 10^9 \text{ W/cm}^2$ , but its rate of decline is faster, so the time to maintain efficient material removal is shorter.

After precision profiling, the contour accuracy and surface micro-

topography of grinding wheels were observed, and the results are shown in Fig. 16. The arc radii of convex/concave grinding wheels were about 4990  $\mu\text{m}$  and 4989  $\mu\text{m}$ , respectively, and the contour errors were

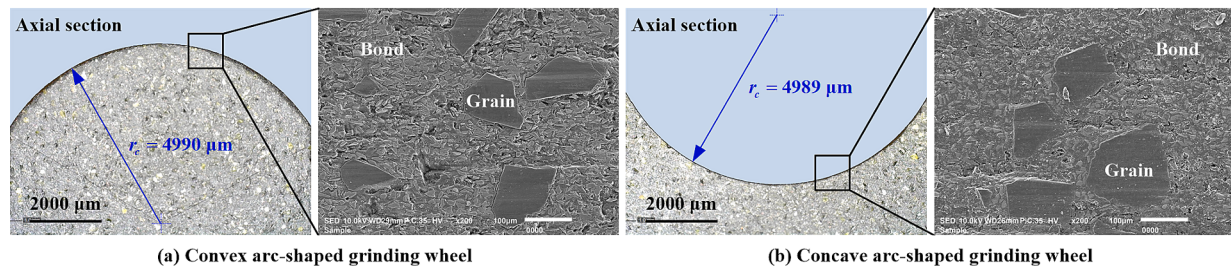


Fig. 16. Surface contour and topography of arc-shaped grinding wheel after profiling.

10 μm and 11 μm, respectively. Similar to the surface of the V-shaped grinding wheel in Fig. 11, the grains and bond were flattened by the laser beam, and the surface flatness of the arc-shaped grinding wheel was very high, and the phenomenon of large grains falling off directly had not been observed. The above research showed that the trajectory planning method was also suitable for convex/concave arc-shaped grinding wheels and had a significant effect in improving the efficiency of laser profiling.

### 3.3.2. Influence of arc radius and chord-to-diameter ratio on profiling efficiency

The arc radius and chord-to-diameter ratio (the value is the ratio of the chord length  $L_c$  to the diameter of the arc) will affect the distribution of laser energy on the surface of the grinding wheel. In this section, we will take the concave arc-shaped grinding wheel as an example to explore the influence of arc radius and chord-to-diameter ratio on trajectory planning and profiling efficiency. The surface of the grinding wheel located to the right of the Y-axis was selected for analysis. When the focal plane passed through point  $A_0$  (Fig. 13(b)) and the laser beam with a power of 70 W scanned along the trajectory line CA (Fig. 14(b)), the laser power density  $I_A$  at each point on the intersection line of the grinding wheel surface was calculated under the conditions of different arc radius  $r_c$  (0.5–25 mm) and chord-to-diameter ratio  $\delta$  (0.1–1), the results are shown in Fig. 17. It could be found that when the laser beam scanned from point C to point A,  $I_A$  showed a downward trend, so the material removal efficiency in the middle area of the grinding wheel surface was higher than that in the edge area. In addition, the larger the  $r_c$  or  $\delta$ , the larger the peak value of  $I_A$ , the smaller the valley value, and the larger the reduction, so the trajectory planning method will improve the profiling efficiency more. For concave arc-shaped grinding wheels with different  $r_c$  and  $\delta$ , different process strategies could be adopted. When  $r_c$  and  $\delta$  were small, high-power laser beams could be used for profiling throughout the process to ensure a high material removal rate and surface contour accuracy. When  $r_c$  and  $\delta$  were large, the laser power should not be too high at the initial stage of profiling so as not to cause too serious damage to the abrasive layer due to too high  $I_A$ ; as the profiling process proceeded, the laser power was gradually increased to obtain higher profiling efficiency and accuracy.

## 4. Conclusions

Aiming at the bottleneck of low laser profiling efficiency of super-abrasive profile grinding wheels, this paper took the evolution law of laser energy on the surface of the grinding wheel as an entry point, analyzed the root causes of low profiling efficiency for the first time,

innovatively proposed a trajectory planning method for deep-cutting laser profiling, and comprehensively explored the improvement effect of this method on the profiling efficiency of V-shaped and arc-shaped resin-bonded diamond grinding wheels and the influence of the sectional contour size and grain size of the grinding wheel on the efficiency improvement. The main conclusions are as follows:

- (1) The theoretical model of the energy distribution of the Gaussian laser beam on the irradiated area of the profile grinding wheel surface was constructed, and the removal threshold of the grinding wheel material was determined by means of the plasma spectrum monitoring method, and then the profiling trajectory planning of the V-shaped and arc-shaped grinding wheels was realized, and the accuracy of the trajectory division was verified. In addition, the method was also applicable to profile grinding wheels with other sectional contour by simply substituting the laser scanning trajectory equation.
- (2) Compared with the entire trajectory scanning method, the segmented trajectory scanning method could effectively improve the profiling efficiency of the V-shaped grinding wheel, and the smaller the tip angle, the greater the improvement in the profiling efficiency of the trajectory planning method. With the decrease of the grain size, the grain removal method gradually changed from crushing removal to falling-off removal, and the profiling efficiency of the V-shaped grinding wheel gradually increased, but the laser profiling accuracy was little affected by the grain size. The laser method could profile the tip arc radius of the V-shaped diamond grinding wheel with a grain size of 180 μm to 18.4 μm, showing incomparable advantages over mechanical or electrical dressing methods.
- (3) The trajectory planning method could also significantly improve the profiling efficiency of the convex/concave arc-shaped grinding wheel, and the larger the arc radius or chord-to-diameter ratio, the greater the improvement of the profiling efficiency by this method. When profiling convex/concave wheels of the same size, the latter had a higher material removal rate, but its profiling time was longer because the volume of material to be removed was also greater. When the arc radius or chord-to-diameter ratio of the grinding wheel was different, it was recommended to choose different profiling process strategies. When they were small, a high-power laser beam could be used throughout, while when they were large, a strategy of gradually increasing the laser power from low to high could be used.

In future research, new online monitoring methods for laser dressing

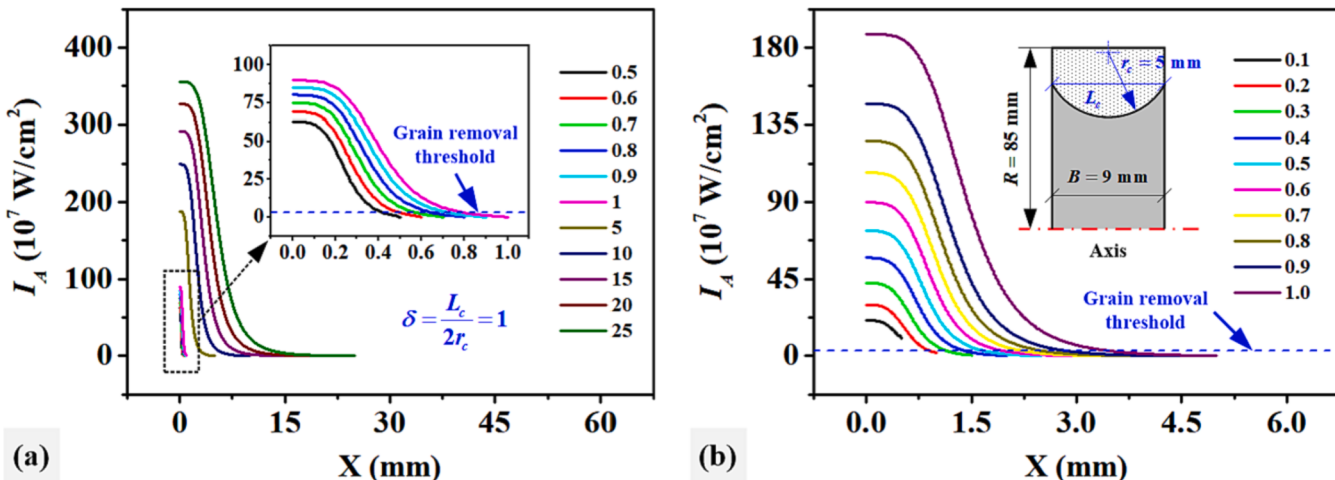


Fig. 17. Influence of (a) arc radius and (b) chord-to-diameter ratio on laser power density.

based on visual measurement and spectral analysis can be further developed to achieve automated dressing of superabrasive profile grinding wheels.

## Declaration of Competing Interest

The authors declare that they have no known competing financial interests or personal relationships that could have appeared to influence the work reported in this paper.

## Acknowledgments

Financial support for this research was provided by the National Natural Science Foundation of China (No. 51975209, No. 52375425), the Science and Technology Innovation Program of Hunan Province (No. 2022RC1136), the Special Projects of the Central Government in Guidance of Local Science and Technology Development (No. 2023ZYC006), and the Scientific Research Fund of Hunan Provincial Education Department (No. 21B0458).

## References

- [1] Z.C. Zhao, N. Qian, W.F. Ding, Y. Wang, Y.C. Fu, Profile grinding of dz125 nickel-based superalloy: grinding heat, temperature field, and surface quality, *J. Manuf. Process.* 57 (2020) 10–22, <https://doi.org/10.1016/j.jmapro.2020.06.022>.
- [2] B. Zhao, X.F. Lei, T. Chen, W.F. Ding, Y.C. Fu, J.H. Xu, H. Li, Simulation and intelligent control during grinding process for difficult-to-machine materials in aerospace, *Diam. Abras. Eng.* 43 (2023) 127–143, <https://doi.org/10.13394/j.cnki.jgszz.2023.1002>.
- [3] H. Deng, Z. Xu, Laser-dressing topography and quality of resin-bonded diamond grinding wheels, *Opt. Laser. Eng.* 136 (2021), 106322, <https://doi.org/10.1016/j.optlaste.2020.106322>.
- [4] N.C. Deresse, V. Deshpande, I.W.R. Taifa, Experimental investigation of the effects of process parameters on material removal rate using taguchi method in external cylindrical grinding operation, *Eng. Sci. Technol. Int. J.* 23 (2020) 405–420, <https://doi.org/10.1016/j.jestech.2019.06.001>.
- [5] K. Wegener, H.W. Hoffmeister, B. Karpuschewski, F. Kuster, W.C. Hahmann, M. Rabiey, Conditioning and monitoring of grinding wheels, *Cirp Ann.-Manuf. Techn.* 60 (2011) 757–777, <https://doi.org/10.1016/j.cirp.2011.05.003>.
- [6] G.Y. Chen, S.Z. Lan, Y.Y. Wang, Z.O.U. Yang, W. Zhou, M.Q. Li, J. Li, Development of cam system for automatic compound dressing of superabrasive grinding wheels, *Diam. Abras. Eng.* 43 (2023) 66–74, <https://doi.org/10.13394/j.cnki.jgszz.2022.0061>.
- [7] J. Yan, S. Li, Z. Yang, B. Chen, W. Cai, L. Zhou, Q. He, J. Chen, W. Fang, Feasibility study on sharpening metal-bond metal diamond grinding tool by microwave-induced electric discharge machining, *Ceram. Int.* 49 (2023) 8952–8961, <https://doi.org/10.1016/j.ceramint.2022.11.050>.
- [8] B. Guo, Q.L. Zhao, On-machine dry electric discharge truing of diamond wheels for micro-structured surfaces grinding, *Int. J. Mach. Tool. Manuf.* 88 (2015) 62–70, <https://doi.org/10.1016/j.ijmachtools.2014.09.011>.
- [9] L.Z. Dai, G.Y. Chen, M.Q. Li, S.Y. Yuan, Experimental study on dressing concave trapezoidal diamond grinding wheel by electrical discharge grinding method, *Diam. Relat. Mater.* 128 (2022), 109218, <https://doi.org/10.1016/j.diamond.2022.109218>.
- [10] S. Wang, Q.L. Zhao, B. Guo, Wear characteristics of electroplated diamond dressing wheels used for on-machine precision truing of arc-shaped diamond wheels, *Diam. Relat. Mater.* 129 (2022), 109372, <https://doi.org/10.1016/j.diamond.2022.109372>.
- [11] B. Guo, Q. Meng, S. Li, G. Wu, Y. Xiang, Q. Zhao, Pulse laser precision truing of the V-shaped coarse-grained electroplating CBN grinding wheel, *Mater. Des.* 217 (2022), 110650, <https://doi.org/10.1016/j.matdes.2022.110650>.
- [12] C. Dold, R. Transchel, M. Rabiey, P. Langenstein, C. Jaeger, F. Pude, F. Kuster, K. Wegener, J. van Griethuysen, A study on laser touch dressing of electroplated diamond wheels using pulsed picosecond laser sources, *Cirp Ann.-Manuf. Techn.* 60 (2011) 363–366, <https://doi.org/10.1016/j.cirp.2011.03.117>.
- [13] H. Deng, X. Wu, G. Yuchi, G. Liu, Z. Xu, J. Yi, Research on laser preparation and grinding performance of hydrophilic structured grinding wheels, *Ceram. Int.* 49 (2023) 7649–7661, <https://doi.org/10.1016/j.ceramint.2022.10.240>.
- [14] O. Bialas, A.N.S. Appiah, M. Wala, A. Kunwar, A. Woźniak, P.M. Nuckowski, W. Simka, P. Raback, M. Adamiak, Laser assisted fabrication of mechanochemically robust Ti3Au intermetallic at Au-Ti interface, *Eng. Sci. Technol. Int. J.* 42 (2023), 101413, <https://doi.org/10.1016/j.jestch.2023.101413>.
- [15] W. Zhou, G.Y. Chen, H.J. Pan, F.R. Luo, Y. Wei, M.Q. Li, Laser precision profiling of small-angle bevel-edge contour grinding wheels, *J. Mater. Process. Technol.* 305 (2022), 117591, <https://doi.org/10.1016/j.jmatprotec.2022.117591>.
- [16] W. Zhou, G. Chen, M. Gao, Y. Wang, Y. Wei, W. Li, Laser machining and compensation truing of small concave-arc bronze-bonded diamond grinding wheels, *J. Manuf. Process.* 79 (2022) 815–826, <https://doi.org/10.1016/j.jmapro.2022.05.016>.
- [17] W. Zhou, G. Chen, H. Pan, K. Cao, F. Luo, Y. Wei, M. Li, Dual-laser dressing concave rectangular bronze-bonded diamond grinding wheels, *Diam. Relat. Mater.* 123 (2022), 108830, <https://doi.org/10.1016/j.diamond.2022.108830>.
- [18] N. Ramesh Babu, V. Radhakrishnan, Y.V.G.S. Murty, Investigations on laser dressing of grinding wheels—part i: preliminary study, *J. Eng. Ind.* 111 (1989) 244–252, <https://doi.org/10.1115/1.3188756>.
- [19] N. Ramesh Babu, V. Radhakrishnan, Investigations on laser dressing of grinding wheels—part ii: grinding performance of a laser dressed aluminum oxide wheel, *J. Eng. Ind.* 111 (1989) 253–261, <https://doi.org/10.1115/1.3188757>.
- [20] C. Walter, M. Rabiey, M. Warhanek, N. Jochum, K. Wegener, Dressing and truing of hybrid bonded CBN grinding tools using a short-pulsed fibre laser, *Cirp Ann.-Manuf. Techn.* 61 (2012) 279–282, <https://doi.org/10.1016/j.cirp.2012.03.001>.
- [21] N. Ackert, M. Warhanek, J. Gysel, K. Wegener, Ultra-short pulsed laser conditioning of metallic-bonded diamond grinding tools, *Mater. Des.* 189 (2020), 108530, <https://doi.org/10.1016/j.matdes.2020.108530>.
- [22] H. Deng, G.Y. Chen, J. He, C. Zhou, H. Du, Y.Y. Wang, Online, efficient and precision laser profiling of bronze-bonded diamond grinding wheels based on a single-layer deep-cutting intermittent feeding method, *Opt. Laser Technol.* 80 (2016) 41–50, <https://doi.org/10.1016/j.optlastec.2015.12.021>.
- [23] H. Deng, Z. Xu, Laser dressing of arc-shaped resin-bonded diamond grinding wheels, *J. Mater. Process. Technol.* 288 (2021), 116884, <https://doi.org/10.1016/j.jmatprotec.2020.116884>.
- [24] A. Mahrle, E. Beyer, Theoretical aspects of fibre laser cutting, *J. Phys. D Appl. Phys.* 42 (2009), 175507, <https://doi.org/10.1088/0022-3727/42/17/175507>.
- [25] A.V. Zaitsev, O.B. Kovalev, A.M. Orishich, V.M. Fomin, Numerical analysis of the effect of the tem00 radiation mode polarisation on the cut shape in laser cutting of thick metal sheets, *Quantum Electron.* 35 (2005) 200–204, <https://doi.org/10.1070/QE2005v03n02ABEH002728>.
- [26] H. Qi, J. Mazumder, H. Ki, Numerical simulation of heat transfer and fluid flow in coaxial laser cladding process for direct metal deposition, *J. Appl. Phys.* 100 (2006), 24903, <https://doi.org/10.1063/1.2209807>.
- [27] A. Zahedi, B. Azarhoushang, J. Akbari, Conditioning of vitrified and resin bond CBN grinding wheels using a picosecond laser, *Sci. Iran.* 24 (2017) 2369–2378, <https://doi.org/10.24200/sci.2017.4307>.
- [28] J. Xie, H.F. Xie, M.J. Luo, T.W. Tan, P. Li, Dry electro-contact discharge mutual-wear truing of micro diamond wheel v-tip for precision micro-grinding, *Int. J. Mach. Tool. Manuf.* 60 (2012) 44–51, <https://doi.org/10.1016/j.ijmachtools.2012.05.006>.